INTERNATIONAL JOURNAL FOR NUMERICAL METHODS IN FLUIDS, VOL. 18, 821–842 (1994)

FINITE ELEMENT ANALYSIS OF MULTICOMPONENT TWO-PHASE FLOWS WITH INTERPHASE MASS AND MOMENTUM TRANSPORT

P. R. SCHUNK AND R. R. RAO

Department of Computational Fluid Dynamics, Sandia National Laboratories, Albuquerque, NM 87185, U.S.A.

SUMMARY

The application of the finite element method to multiphase flow problems with interphase mass and heat transfer is described. A general formulation is used that determines the position of the interfacial boundary and allows for multiple solvents, differential volatilities and concentration- and temperature-dependent thermophysical properties. Species phase change and the dramatic volume change that accompanies interphase mass transfer make implementation of the theory challenging, since these events lead to discontinuous velocities and concentrations at phase boundaries. These discontinuities are especially large in processes involving rapid evaporation or condensation. As examples we examine the effects of rapid drying on film and fibre formation of sol–gel materials, which are often laden with volatile species.

KEY WORDS Free-surface Interphase mass transfer Finite element two-phase flow Coating

1. INTRODUCTION

Fluid mechanics problems that are coupled with evaporation and condensation phenomena in processes such as boiling, distillation and drying have yet to be modelled in detail with any numerical method. Numerical analyses of *free surface flows* have usually been made with little or no consideration of interphase mass and heat transport. Exceptions include several analyses that employ mass and heat transfer coefficients as expedients to a complete multiphase flow theory.[1,2] In most cases these coefficients are empirical or are derived from overly simplified theories in one or more phases.

When a transfer coefficient model is applied to one phase, the transport mechanisms in that phase are lumped into three variable coefficients, one for each transfer field, i.e. heat, mass and momentum. Thus the governing equations need only be solved in the remaining phases, thereby greatly reducing the size and complexity of the problem. Transfer coefficients can be obtained experimentally but are more often obtained from simplified theories such as boundary layer models.[3] These coefficients in many cases adequately represent the transport phenomena of interest and have been used successfully in the analysis of interphase transport.[1,4] However, when mass and heat transfer rates across interfaces are rapid enough to alter the flow field significantly, classical heat and mass transfer theories are often inaccurate unless they can be corrected for the effect of transfer rate.[3] Moreover, any change in the flow, mass or heat transfer field in that phase must be figured into these coefficients, which can sometimes be handled by modification of the simplified theory but more often makes those theories analytically intractable. If adequate transfer coefficients are inaccessible, the only alternative is to solve the governing equations in both phases.

CCC 0271–2091/94/090821–22

Received 17 April 1993
Revised 1 November 1993

The shortcomings of mass and heat transfer theory are nowhere more evident than in solvent removal from films and fibres.[1,5,6] Coating films and spinning fibres of advanced sol–gel (ceramic) materials, for example, require precise drying control and hence complete knowledge of the details of the heat, mass and momentum transport fields in both phases. We happen to use these examples as case studies in this paper, but analysis of any process that involves interphase mass transport can potentially benefit from the approach we take here.

Unfortunately, multicomponent solvent mixtures and multiple phases complicate conventional numerical techniques for analysing multiphase flows. A critical complexity is the volume change which accompanies phase change, which is normally 1000-fold for liquid-to-gas transitions. Thus, if we consider the interface to be a surface in space incapable of holding any significant mass inventory, the velocity will be dual-valued in order to accommodate mass conservation. Moreover, the concentrations of each species present in both phases are in general discontinuous at the interface because of the principles of vapour–liquid equilibrium.[7] In essence, the interface represents a shock in velocity and concentration and hence requires special treatment. Interestingly, the same is not true of the temperature field, which is most realistically taken to be continuous at the interface although subject to Stefan-life flux conditions.

The paper is organized as follows. Section 2 focuses on the complete theory necessary to describe the evaporation and condensation processes in multiphase viscous free surface flows; film and fibre formation processes are used as examples in this development. Section 3 describes the implementation of the theory in a free surface code based on the Galerkin finite element method, elliptic subdomaining and a standard free boundary technique for determining the location of the free surface. Finally we consider two case studies in sol–gel processing to which we apply the complete two-phase flow theory (Section 4). In Section 5 the results are validated against measurements of concentration along films and fibres. We also compare modelling results from the full two-phase multicomponent theory with simplified modelling results using transfer coefficients in the gas phase.

2. THEORY OF FREE SURFACE FLOW WITH EVAPORATION AND CONDENSATION

Vaporization or condensation phenomena complicate conventional analysis of free surface flows: the most simplified but realistic theory must include convective diffusion together with the Navier–Stokes system and all boundary conditions common to free surface flows. The purpose of this section is to augment existing theories, e.g. the work of Scriven and co-workers,[8,9] to account for interphase transfer of multicomponent solvents, differential evaporation an condensation and surface tension gradients, thereby enabling the realistic analysis of drying in coating and fibre-spinning processes. Although most drying theories available today include the coupled momentum, energy and species transport in the liquid phase, they lump the same theory for the gas phase into mass transfer coefficients.[4,10,11] This was our initial approach, but we found no available theory for mass transfer in the gas phase to be adequate (see Section 5). We therefore proceeded to analyse the coupled physics in both phases, employing the proper interphase boundary conditions. Although we happen to focus on coating and fibre-spinning processes (Figure 1), the development below pertains to any related flow.

Two-phase multicomponent systems

Here we allow for up to three components in both the liquid and gas, with each phase having a constant density. All other material properties are allowed to vary. Incompressible

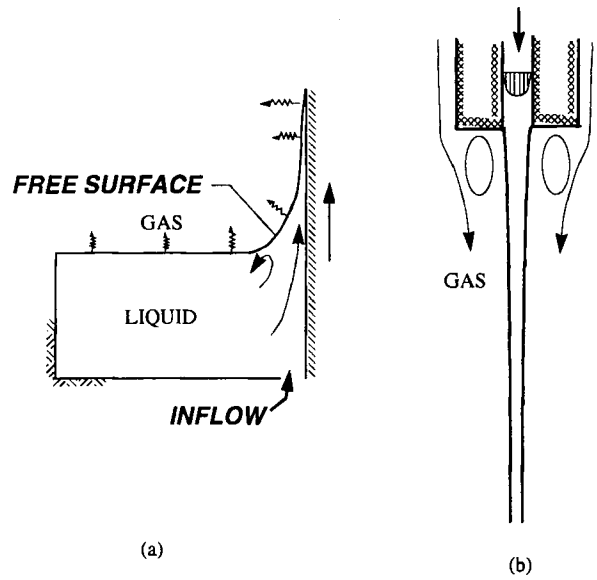

Figure 1: Computational domans of (a) dip coating and (b) fibre spinning (extrusion)

flow in the gas and liquid phases is governed by the principles of conservation of momentum and mass, i.e.

$$\rho\left(\frac{\partial u}{\partial t} + \mathbf{u}\cdot\nabla\mathbf{u}\right) = \nabla\cdot\mathbf{T} + \mathbf{f}, \tag{1}$$

$$\nabla\cdot\mathbf{u} = 0. \tag{2}$$

Here $\mathbf{u}$ is the mass-averaged velocity, ρ is the density, $\mathbf{T} \equiv -\mathbf{I}_p + \eta[\nabla\mathbf{u} + \nabla\mathbf{u})^{\mathrm{T}}]$ is the stress tensor for a generalized Newtonian liquid, where $\mathbf{I}$ is the unit tensor, η is the viscosity and p is the hydrodynamic pressure, and $\mathbf{f}$ is the body force per unit volume. For non-isothermal systems an energy equation is also needed:

$$\rho C_{\mathrm{p}}\left(\frac{\partial T}{\partial t} + \mathbf{u}\cdot\nabla T\right) = \nabla\cdot k\nabla T. \tag{3}$$

Here C_{p} is the heat capacity and k is the thermal conductivity. In addition to the Navier-Stokes system and the energy equation, convective diffusion equations can be written for each component in each phase, assuming no reactions and constant density:

$$\frac{\partial X_i}{\partial t} + \mathbf{u}\cdot\nabla X_i = -\nabla\cdot j_i \quad \text{for } i = 1, 2, 3. \tag{4}$$

Here X_i is the bulk mass fraction of species i and $\mathbf{j}_i$ is given by Fick's law of diffusion, i.e. $\mathbf{j}_i \equiv -\rho D_i \nabla X_i$, where D_i is the pseudobinary diffusivity of species i. The equation of overall mass conservation, i.e. the continuity equation (2), which is already part of the Navier–Stokes system, is used in place of one of the components of equation (4).

The convective diffusion equations for species transport can alter bulk fluid motion in several ways. First, diffusion itself can induce mass-averaged motion and hence influence the balance of

momentum, although this effect is not present with the constant densities we assume here. Second, evaporation or condensation at a free surface introduces fluid motion in the bounding phases and can actually alter the surface shape owing to the momentum imparted by the volume change. Third, the liquid composition at the free surface can be altered by species transport, thereby leading to localized surface tension variations. This upsets the balance of forces at the free surface: local excursions of surface tension away from its equilibrium value affect the normal balance of forces, while variations in surface tension along the surface affect the tangential balance of forces. These effects are accounted for in the boundary conditions applied at the free surfaces.

Boundary and interphase conditions for multicomponent multiphase flow

In this work all fluids are assumed to adhere and be impermeable to all solid boundaries so that the so-called no-slip and impenetrable boundary conditions apply. At all inflow and outflow boundaries either a condition prescribing velocities (fully developed velocity profile known *a priori*), a condition of vanishing normal traction in combination with one prescribed velocity component (fully developed) or a condition of vanishing surface stress is applied. It is important to note that the incoming or outgoing volumetric flow rate may not be known *a prior* when a free boundary intersects an inflow or outflow boundary. In that case the prescribed velocity profile must be parameterized by an effective film thickness. This occurs in the dip-coating process we analyse in Section 4.

When mass exchange is allowed across the free surface, the velocity there will be discontinuous if the material undergoes a density change. In two dimensions, at a given locale on the free surface there will be four velocity components from a double-valued velocity vector. The corresponding conditions needed to determine these components are

$$\mathbf{n}\cdot\mathbf{T}|_{\mathrm{l}} = \mathbf{n}\cdot\mathbf{T}|_{\mathrm{g}} + 2H\sigma\mathbf{n} + \mathbf{n}\cdot\rho^{\mathrm{l}}(\mathbf{u}^{\mathrm{l}} - \mathbf{u}_{\mathrm{s}})(\mathbf{u}^{\mathrm{l}} - \mathbf{u}^{\mathrm{g}}) + \nabla_{\mathrm{s}}\sigma, \tag{5}$$

$$\mathbf{t}\cdot\mathbf{u}|_{\mathrm{g}} = \mathbf{t}\cdot\mathbf{u}|_{\mathrm{l}}, \tag{6}$$

$$\rho^{\mathrm{g}}(1 - X_1^{\mathrm{g}} - X_2^{\mathrm{g}})\mathbf{n}\cdot(\mathbf{u} - \mathbf{u}_{\mathrm{s}}) = -\rho^{\mathrm{g}}\nabla D^{\mathrm{g}}(X_1^{\mathrm{g}} + X_2^{\mathrm{g}}), \tag{7}$$

where $\mathbf{n}$ represents the unit normal vector to the surface, $\mathbf{t}$ represents the unit tangent vector to the same; σ is the surface tension and $2H$ is the mean curvature of the surface. The vector condition (5) is applied as a boundary condition on the Navier-Stokes equations in the liquid phase, while the scalar conditions (6) and (7) are applied as boundary conditions on the Navier–Stokes equations in the gas phase. The superscripts 'l' and 'g' denote liquid phase and gas phase respectively.

Equation (5) is a vector condition that balances the normal and tangential components of the viscous forces and the hydrodynamic pressure in both adjacent phases with the capillary pressure, the vapour recoil by volume expansion and the surface tension gradients at the interface. Equation (6) enforces the continuity of tangential velocity at the interface. Equation (7) expresses the gas phase velocity component normal to the interface as a function of the gradients in concentration in the gas phase next to the surface. It is derived on the premise that the Nth component in the gas is effectively insoluble in the liquid. In this work the insoluble component is taken to be air. All other volatile components are allowed to enter the gas phase by evaporation or to re-enter the liquid phase by condensation. Equation (7) can be replaced by a similar condition written for the liquid phase.

Boundary conditions on the energy equation (3) are

$$\mathbf{n} \cdot \nabla T = 0 \quad \text{at solid surfaces,} \tag{8}$$

$$T^{\mathrm{l}} = T^{\mathrm{g}} \quad \text{at free surfaces,} \tag{9}$$

$$k^{\mathrm{l}} \mathbf{n} \cdot \nabla T^{\mathrm{l}} = k^{\mathrm{g}} \mathbf{n} \cdot \nabla T^{\mathrm{g}} + \sum_{i=1}^{n} \mathbf{n} \cdot \rho^{\mathrm{l}} (\mathbf{u}^{\mathrm{l}} - \mathbf{u}_{\mathrm{s}}) X_i \Delta H_i^{\mathrm{vap}} \quad \text{at free surfaces,} \tag{10}$$

where $\Delta H_i^{\mathrm{vap}}$ is the latent heat of vaporization per unit mass of volatile component i. The first condition (equation (8)) states that no flux is allowed at solid surfaces. Equation (9) enforces continuous temperature at interface boundaries; this condition is auxiliary to equation (10), which is a Stefan condition that balances the jump in heat flux with the latent heat release or adsorption for vaporizing or condensing mass at the same boundaries. Prescribed temperatures are used at all inflow boundaries as conditions on the energy equation (3). Also, we are careful to place all outflow planes far enough downstream that we can apply conditions such as equation (8).

Boundary conditions on the convective diffusion equations (4) are

$$\mathbf{n} \cdot \nabla X_i = 0 \quad \text{for } i = 1, 2, 3 \quad \text{at solid surfaces,} \tag{11}$$

$$\mathbf{n} \cdot [(\mathbf{u}_{\mathrm{s}} - \mathbf{u}^{\mathrm{l}}) X_i^{\mathrm{l}} \rho^{\mathrm{l}} - \mathbf{j}_i^{\mathrm{l}}] = \mathbf{n} \cdot [(\mathbf{u}_{\mathrm{s}} - \mathbf{u}^{\mathrm{g}}) X_i^{\mathrm{g}} \rho^{\mathrm{g}} - \mathbf{j}_i^{\mathrm{g}}] \quad \text{for } i = 1, 2, 3 \quad \text{at free surfaces,} \tag{12}$$

where $\mathbf{j}_i$ is the diffusive contribution to the total flux $\mathbf{n}_i \equiv \rho X_i \mathbf{u} + \mathbf{j}_i$ of species i and $\mathbf{u}_{\mathrm{s}}$ is the velocity of the free surface. Equation (11) implies that solid surfaces are impermeable to all species. Equation (12) allows free surfaces to exchange species: the diffusive and convective flux of component i normal to the surface in the liquid must be balanced by the diffusive and convective flux of component i normal to the surface in the gas. Here we assume that the surface is incapable of holding a significant inventory of any species in excess of the bulk under equilibrium conditions, i.e. no species here is taken to be surface-active.[12] The species in the liquid that are taken as non-volatile and the species in the gas that are taken as insoluble in the liquid are accounted for by no-penetration conditions at the free surface of the form $\mathbf{n}_i = \rho X_i \mathbf{u} + \mathbf{j}_i = 0$.

Analogously to the bulk equations above, we replace one of the species kinematic conditions (equation (12)) with a condition formed by summing the component equations of equation (12). The result is a condition that enforces the overall mass flux across the surface to be continuous, i.e. the so-called kinematic boundary condition

$$\mathbf{n} \cdot (\mathbf{u}^{\mathrm{l}} - \mathbf{u}_{\mathrm{s}}) \rho^{\mathrm{l}} = \mathbf{n} \cdot (\mathbf{u}^{\mathrm{g}} - \mathbf{u}_{\mathrm{s}}) \rho^{\mathrm{g}}. \tag{13}$$

The remaining boundary conditions needed on equation (4) must provide a datum which sets a concentration level for each species. That datum can be set at an inflow boundary, as it usually is in the liquid phase:

$$X_i = X_i^0 \quad \text{at inflow surfaces.} \tag{14}$$

Equation (14) might apply in the gas phase if gas of a known saturation is blown into the system. Otherwise the datum is set at the interface with the conditions on vapour–liquid equilibrium.

The solvent in the gas phase at the free surface is taken to be in equilibrium with the solvent in the liquid at the free surface. In this work we approximate this equilibrium behaviour by Raoult's law

$$p_i = p_i^V \tilde{x}_i|_h, \tag{15}$$

where p_i^V is the saturation vapour pressure of solvent component i at a specific temperature, $\tilde{x}_i$ is the mole fraction of the same in the liquid at the free surface and p_i is the partial pressure of component i in the gas phase at the free surface. Raoult's law usually holds for the component present in excess or when the system can be taken as thermodynamically ideal. For many systems, however, Raoult's law is satisfactory over a wide range of concentrations.[7] We plan on taking this simplified approach until there is reason to believe that a more sophisticated model is necessary to predict the experimental data.

The vapour pressures of the volatile species are temperature-sensitive. If we assume that the solution is ideal, i.e., that each component behaves as if it were pure, then we can represent this temperature sensitivity by the Clausius–Clapeyron equation[7]

$$\frac{\mathrm{d}}{\mathrm{d}T} p_i^V = \frac{\Delta \tilde{H}_i^{\mathrm{vap}}}{T(\tilde{V}^{\mathrm{g}} - \tilde{V}^{\mathrm{l}})}, \tag{16}$$

where $\Delta \tilde{H}_i^{\mathrm{vap}}$ is the molar heat of vaporization of component i, $\tilde{V}^{\mathrm{g}}$ is the molar volume of the gas and $\tilde{V}^{\mathrm{l}}$ is the molar volume of the liquid. Equation (16) can be integrated if we assume that the molar volume of the liquid is negligible compared with that of the gas and that the gas behaves ideally.[13] This yields

$$\log p_i^V = -\frac{\Delta \tilde{H}_i^{\mathrm{vap}}}{RT} + B, \tag{17}$$

where R is the gas constant and B can be determined from experimental vapour pressure data. Equation (17) is best used over small temperature ranges near the range for which the data used to determine B are valid.[13]

To make equation (15) computationally convenient, we express p_i in terms of the mole fraction $\tilde{x}_i$ in the gas phase by Dalton's law $p_i/p_{\mathrm{tot}} = \tilde{x}_i^{\mathrm{g}}$. The remaining challenge is to convert mass fractions into mole fractions so that equations (4) and (5) can be used together with equation (15). This can be accomplished by solving all but one of the following definition equations for the mole fraction of component i,

$$X_i = \frac{\tilde{x}_i M_i}{\tilde{x}_1 M_1 + \tilde{x}_2 M_2 + \tilde{x}_3 M_3} \quad \text{for } i = 1, 2, 3, \tag{18}$$

together with the constraint that $\tilde{x}_1 + \tilde{x}_2 + \tilde{x}_3 = 1$. An alternative to solving equation (18) is to use a volume-fraction-based formulation, a situation for which Amagat's law states that volume fractions equal mole fractions in ideal gases.

3. COMPUTATIONAL STRAGEGIES FOR SIMULTANEOUS MOMENTUM AND SPECIES TRANSPORT

Solution procedure

We use a procedure based on the earlier works of Christodoulou and Scriven[8] to solve the system of equations outlined in Section 2. The techniques are based on the method of subdomaining with convenient finite element basis functions (biquadratic basis functions for velocity, concentration and temperature, bilinear basis functions for pressure on subparametric quadrilateral elements), Galerkin's method of weighted residuals and Gaussian quadrature. The subdomain structure or mesh is designed with an elliptic generation scheme.[8] In this scheme the kinematic boundary condition (13) is used to replace one of the elliptic partial differential equations governing the movement of the mesh at nodes along the surface. Consequently, meshes are produced that automatically conform to changes in boundary shape when physical parameters are varied. Sample meshes are shown in Figure 2.

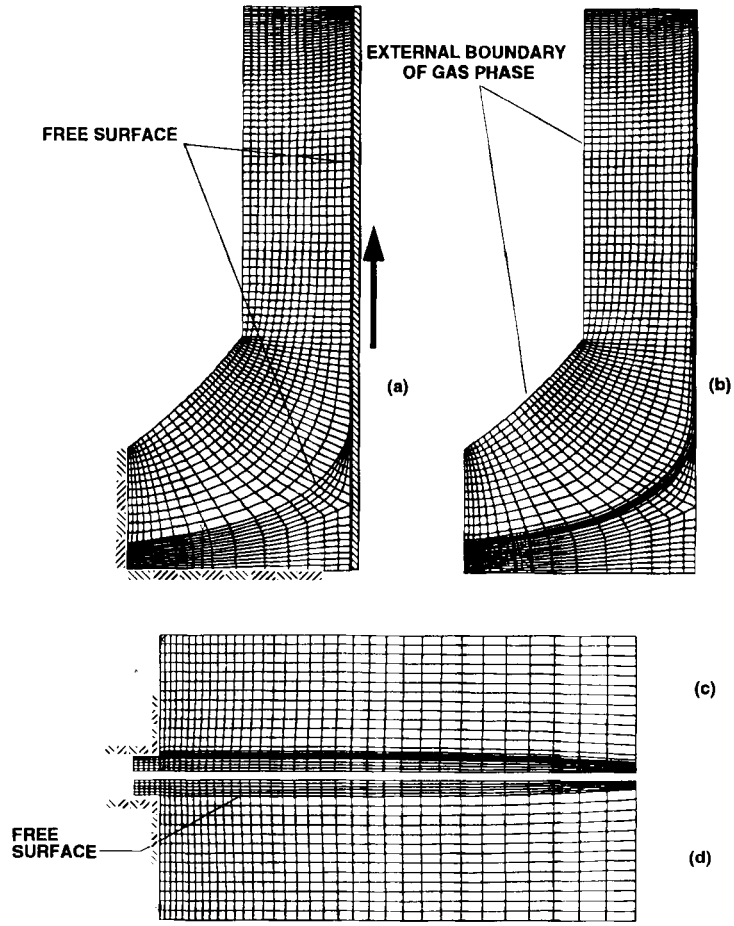

Figure 2. Sample meshes for two-phase flow: (a) dip-coating coarse mesh; (b) dip-coating fine mesh; (c) fibre extrusion fine mesh; (d) fibre extrusion coarse mesh

In order to cope efficiently with the thin boundary layers in concentration that develop next to the free surface, we employ a two-level discretization scheme.[14] A two-level scheme is helpful since boundary layers of momentum and concentration are disparate, with the concentration boundary layers being much thinner in the liquid because solute diffusivities are much smaller than the kinematic viscosity. The problem is not as severe in the gas phase: although momentum boundary layers are in general thinner than in the liquid, diffusivities are roughtly the same magnitude as the kinematic viscosity. Resolving the narrow boundary layers of one field with a single mesh squanders computational work on unwarranted resolution of broad boundary layers of another field, i.e. a discretization fine enough for the concentration field is unnecessarily expensive to resolve the other fields of interest.

In the two-level scheme a fine mesh is designed to cover the concentration boundary layer and to fit into the coarser mesh that suffices for the rest of the flow. The fit facilities interpolation of velocities from the coarse on to the fine mesh of finite elements and projections of the concentration from the latter on to the former. The new scheme handles this in such a way that the entire set of non-linear algebraic equations to which the discretization leads can be solved by Newton's method.

Figure 2 shows a sample of the two levels of discretization used in analysing dip-coating and fibre-spinning processes. The fine level in both cases was formed by algebraically 'subdividing' four times the rows of elements adjacent to the free surface on either side of the interface, with a geometric progression in element thickness perpendicular to the free surface. The meshes shown in Figures 2(a) and 2(b) contain 1883 biquadratic elements in the coarse grid and 2435 biquadratic elements in the fine grid and give rise to a total of 46,394 unknown coefficients for ternary systems in both phases. The meshes shown in Figures 2(c) and 2(d) contain 637 biquadratic elements in the coarse grid and 856 biquadratic elements in the fine grid and give rise to a total of 18,127 unknown coefficients.

The discontinuities in velocity and concentration at the free surface due to the volume change on evaporation and vapour–liquid equilibrium were handled with two nodes assigned to the same physical location on the surface. One node was assigned to the liquid phase element and one to the gas phase element. For formation of the weighted residual equations at these nodes is described next.

Weighted residual formation

The formation of the weighted residual equations is often underrated in its complexity. This is especially true when applying the collection of conditions at the free surface which enforce mass, species and momentum conservation. Without mass exchange at the phase boundaries, those boundaries become material lines (two-dimensional) or surfaces (three-dimensional) at which the velocity is continuous. The difficulties begin with unknown concentrations, which in general are discontinuous at phase boundaries by virtue of the phase equilibrium conditions which partition the species between phases. There clearly is a special need for increasing the number of degrees of freedom at nodes lying on the phase boundaries, because the phase equilibrium conditions are often too complex to substitute directly into the equations. In this work we allow several species to exist in both gas and liquid phases, but at any locale on the interface there are two concentrations of each species related in magnitude by vapour–liquid equilibrium. Hence two concentration degrees of freedom at the interface must be tracked for each species unless the species exist in only one phase, i.e. the species is either non-volatile (liquid phase) or insoluble (gas phase). Hence at each computational location (node) we must account for

2 × (number of volatile/soluble species) + (non-volatile/insoluble species in each phase)

unknown concentration degrees of freedom. This means that we must increase the number of degrees of freedom correspondingly at nodes on the free surface or equivalently increase the number of nodes at the same physical location.

To compound the problem, a discontinuity in density occurs at the gas–liquid interface that causes the velocities at the interface to be dual-valued. In order to capture the correct magnitude of the concentration and velocity discontinuities, care must be taken when formulating the residual equations. In the Galerkin finite element method these equations are derived by (i) representing the dependent variables (velocity, pressure, concentrations and temperature) in terms of finite element basis functions, (ii) inserting those representations into the governing equations and (iii) requiring that the weighted residuals of those equations with respect to the same basis functions vanish.[15] The weighted residuals of the momentum equation (1) and the convective diffusion equations (4) are

$$\mathbf{R}_i^{\mathrm{M}} \equiv \int_A \left[\rho\left(\frac{\partial \mathbf{u}}{\partial t} + \mathbf{u}\cdot\nabla\mathbf{u}\right) - \mathbf{f}\right]\phi^i \,\mathrm{d}A + \int_A \mathbf{T}\cdot\nabla\phi^i \,\mathrm{d}A - \int_{\partial A} \phi^i(\mathbf{n}\cdot\mathbf{T})\,\mathrm{d}s = 0, \tag{19}$$

$$R_i^{\mathrm{C}} \equiv \int_A \left(\frac{\partial X_i}{\partial t} + \mathbf{u}\cdot\nabla X_i\right)\phi^i \,\mathrm{d}A + \int_A \nabla\phi^i\cdot\mathbf{j}_i \,\mathrm{d}A - \int_{\partial A} \phi^i(\mathbf{n}\cdot\mathbf{j}_i)\,\mathrm{d}s = 0, \tag{20}$$

Where A is the computational domain, ∂A is its boundary and ϕ^i is the basis function at node i. Typically these functions are chosen as low-order polynomials which adhere to a set of standard compatibility constraints.[16] Note that the divergence theorem has been applied to the $\nabla\cdot\mathbf{T}$ term in equation (19) (from equation (1)) and the $\nabla\cdot\mathbf{j}_i$ term in equation (20) (from equation (4)). Although not shown, the energy equation (3) is treated in a similar fashion.

In this study we are concerned with the application of these equations at the free boundaries, since it is there that the velocity and concentrations are discontinuous. When applied at the free surface as an equation for a concentration or velocity unknown, the integrals in equations (19) and (20) will receive contributions from elements on either side of the interface. Splitting the integrals between the liquid and gas, we have:

$$\begin{aligned}\mathbf{R}_i^{\mathrm{M}} \equiv{}& \int_{A^{\mathrm{l}}} \left[\rho^{\mathrm{l}}\left(\frac{\partial \mathbf{u}}{\partial t} + \mathbf{u}\cdot\nabla\mathbf{u}\right) - \mathbf{f}\right]\phi^i \,\mathrm{d}A + \int_{A^{\mathrm{l}}} \mathbf{T}^{\mathrm{l}}\cdot\nabla\phi^i \,\mathrm{d}A - \int_{\partial A^{\mathrm{l}}} \phi^i(\mathbf{n}\cdot\mathbf{T}^{\mathrm{l}})\,\mathrm{d}s \\ &+ \int_{A^{\mathrm{g}}} \left[\rho^{\mathrm{g}}\left(\frac{\partial \mathbf{u}}{\partial t} + \mathbf{u}\cdot\nabla\mathbf{u}\right) - \mathbf{f}\right]\phi^i \,\mathrm{d}A + \int_{A^{\mathrm{g}}} \mathbf{T}^{\mathrm{g}}\cdot\nabla\phi^i \,\mathrm{d}A - \int_{\partial A^{\mathrm{g}}} \phi^i(\mathbf{n}\cdot\mathbf{T}^{\mathrm{g}})\,\mathrm{d}s = 0,\end{aligned} \tag{21}$$

$$\begin{aligned}R_i^{\mathrm{C}} \equiv{}& \int_{A^{\mathrm{l}}} \left(\frac{\partial X_i}{\partial t} + \mathbf{u}\cdot\nabla X_i\right)\phi^i \,\mathrm{d}A + \int_{A^{\mathrm{l}}} \nabla\phi^i\cdot\mathbf{j}_i^{\mathrm{l}} \,\mathrm{d}A - \int_{\partial A^{\mathrm{l}}} \phi^i(\mathbf{n}\cdot\mathbf{j}_i^{\mathrm{l}})\,\mathrm{d}s \\ &+ \int_{A^{\mathrm{g}}} \left(\frac{\partial X_i}{\partial t} + \mathbf{u}\cdot\nabla X_i\right)\phi^i \,\mathrm{d}A + \int_{A^{\mathrm{g}}} \nabla\phi^i\cdot\mathbf{j}_i^{\mathrm{g}} \,\mathrm{d}A - \int_{\partial A^{\mathrm{g}}} \phi^i(\mathbf{n}\cdot\mathbf{j}_i^{\mathrm{g}})\,\mathrm{d}s = 0,\end{aligned} \tag{22}$$

where as before the superscripts 'l' and 'g' refer to liquid phase and gas phase quantities respectively. Because $\partial A^{\mathrm{l}} = \partial A^{\mathrm{g}}$ and $\mathbf{n}^{\mathrm{l}} = -\mathbf{n}^{\mathrm{g}}$, equation (5) can be combined with equation (21)

and equation (12) can be combined with equation (22) to give

$$\mathbf{R}_i^{\mathrm{M}} \equiv \int_{(A^{\mathrm{l}}+A^{\mathrm{g}})} \left[\rho^{\mathrm{l}}\left(\frac{\partial \mathbf{u}}{\partial t} + \mathbf{u}\cdot\nabla\mathbf{u}\right) - \mathbf{f}\right]\phi^i \,\mathrm{d}A + \int_{(A^{\mathrm{l}}+A^{\mathrm{g}})} \mathbf{T}^{\mathrm{l}}\cdot\nabla\phi^i \,\mathrm{d}A$$
$$+ \int_{\partial A} \phi^i[2H\sigma\mathbf{n} + \mathbf{n}\cdot\rho^{\mathrm{l}}(\mathbf{u}^{\mathrm{l}} - \mathbf{u}_{\mathrm{s}})(\mathbf{u}^{\mathrm{l}} - \mathbf{u}^{\mathrm{g}}) + \nabla_{\mathrm{s}}\sigma] \,\mathrm{d}s = 0, \tag{23}$$

$$R_i^{\mathrm{C}} \equiv \int_{(A^{\mathrm{l}}+A^{\mathrm{g}})} \left(\frac{\partial X_i}{\partial t} + \mathbf{u}\cdot\nabla X_i\right)\phi^i \,\mathrm{d}A + \int_{(A^{\mathrm{l}}+A^{\mathrm{g}})} \nabla\phi^i\cdot\mathbf{j}_i^{\mathrm{l}} \,\mathrm{d}A$$
$$- \int_{\partial A} \phi^i[\mathbf{n}\cdot(\mathbf{u}_{\mathrm{s}} - \mathbf{u}^{\mathrm{l}})X_i^{\mathrm{l}}\rho^{\mathrm{l}} - \mathbf{n}\cdot(\mathbf{u}_{\mathrm{s}} - \mathbf{u}^{\mathrm{g}})X_i^{\mathrm{g}}\rho^{\mathrm{g}}] \,\mathrm{d}s = 0. \tag{24}$$

Thus at each node along the free surface equation (23), a vector equation, is used to account for either the gas phase velocity components or the liquid phase velocity components, the other two components being accounted for by the weak form of equations (6) and (7). The same procedure is used for each volatile species: equation (24) is used to account for either the liquid or gas concentration and the vapour–liquid equilibrium condition (15) is used to account for the other. Clearly the bookkeeping is more complex than in the case where the velocities and concentrations are continuous at the interface, but conveniently we see no need to evaluate $\mathbf{n}\cdot\mathbf{j}_i$ and $\mathbf{n}\cdot\mathbf{T}$ terms at the interface, which would bring with it some inaccuracy because of the C^0 elements we use, for which only the primitive variables are continuous at element boundaries.

4. APPLICATION TO FORMATION OF SOL–GEL THIN FILMS AND FIBRES

Formation of sol–gel films by dip coating

Sol–gel films have enjoyed recent attention because they are suitable for a wide range of applications.[17] This versatility stems from the wide range of porosity that can be tailored into thin films simply by varying the processing conditions. By 'sol' we mean a colloidal dispersion of particles in a liquid; by 'gel' we mean a giant aggregate or molecule that extends throughout the sol. Typically the particles are inorganic or metal organic precursors which participate in a polymerization (gelation) process. Processing a sol usually includes this gelation stage; dip-coating processes are no exception. Today sol–gel thin film coatings are being studied intensively for such diverse applications as protective and optical coatings, passivation and planarization layers, inorganic membranes, semiconducting antistatic coatings and non-linear optical films, superconducting films, strengthening layers and ferroelectrics. In most of these applications the sol is put down on the substrate by dip coating or a related technique.

Dip coating sol–gel materials involves more than a competition between viscous, capillary and gravitational forces;[18] the mechanism which controls the final film thickness and microstructure is considerably more complex, as shown in Figure 3. Film thinning by gravitational draining is assisted by vigorous evaporation, which also acts to decrease the amount of liquid that can be withdrawn. To make matters even more complicated, sols are typically formulated with several solvents, each of which usually differs in volatility and surface tension. Sometimes the relative volatilities are different enough to lead to differential solvent evaporation and ultimately to concentration variations along the film. Differential evaporation triggers several other events at and beneath the liquid–gas interface. First, it may lead to concentration variations along the gas–liquid interface; these variations cause surface tension gradients which

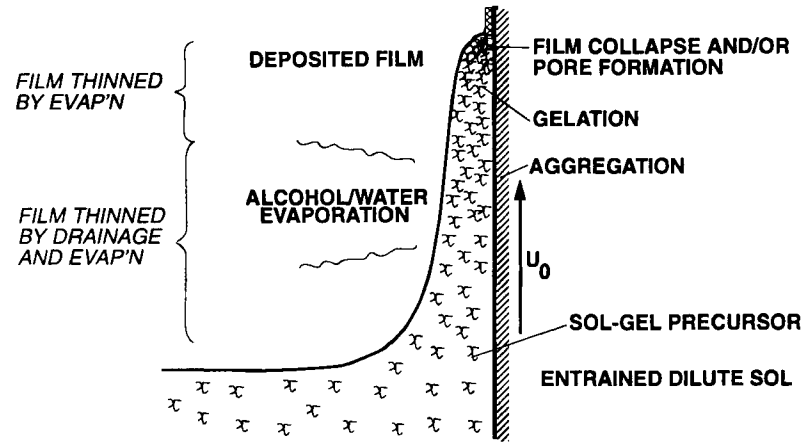

Figure 3. Schematic diagram of steady state dip-coating process showing sequential stages of structural development that result from draining accompanied by solvent evaporation and continued condensation reactions

contribute to the surface stress and alter the flow. Second, differential evaporation leads to the diffusion of volatile species towards the surface and non-volatile species away from the surface.

In our analysis of sol–gel dip coating we concentrate on the effects of differential evaporation and surface tension gradients on the details of film formation. The many thermophysical properties and coater design specifications in Table I define a case of a dip-coating process. A solution of ethanol in water with a dispersed, non-volatile phase was chosen as a model system because it is typical of a silica-based sol. The system is taken as isothermal and the density, viscosity and diffusivity of the liquid and gas are taken to be independent of the concentrations of all species. These restrictions are not imposed in our analysis of fibre formation below.

We will focus here on the effects of surface tension gradients during film formation. Those gradients are caused by differential evaporation from the film into the gas. The surface tension

Table I: Operating conditions and thermophysical properties for dip-coating, base case

Operating conditions	
Liquid composition (volume %)	74:16:10 ethanol/water/non-volatile species
Substrate speed	1·0 cm s^{-1}
Substrate withdrawal angle	Vertical
Reservoir width	7 mm
Reservoir depth	3 mm
Thermophysical properties	
Liquid viscosity	2×10^{-3} Pa s
Gas viscosity	$1{\cdot}8 \times 10^{-5}$ Pa s
Liquid density	1000 kg m^{-3}
Gas density	1 kg m^{-3}
Surface tension (equilibrium 20 °C)	30 mN m^{-1}
Liquid diffusivity	1×10^{-8} m^2 s^{-1}
Gas diffusivity	$1{\cdot}6 \times 10^{-4}$ m^2 s^{-1}

σ is taken here to be a function of concentration alone. What is needed is a constitutive equation that relates the surface tension to the concentration of all components in the liquid next to the surface or at least those components that affect the surface tension. The best constitutive equation arises from fitting a function to the actual data. The surface tensions at various ethanol concentrations are shown in Figure 4. We fitted a hyperbolic cosine functions to the data in the range 0–0·2 mass fraction ethanol and a linear function in the range 0·2–1. The fit served as the constitutive equation for surface tension.

The boundary conditions we impose on the gas flow in the base case force dry air into the domain over a portion of the artificial boundary that overlies the reservoir (see Figure 5). The velocity of the gas over this portion was taken to be 0·1 cm s^{-1}, which is of the order of the substrate speed, i.e. 0·2 cm s^{-1}, but far less than the evaporation-induced velocity in the gas phase (of the order of 10 cm s^{-1}). Over the same portion of the boundary we specified the incoming gas composition to be void of water and ethanol vapour. The remaining external boundary in the gas phase is presumed to be free of viscous traction and of diffusive flux of each species, except for the solid boundary that contains the coating liquid on the left-hand part of the domain, which is taken to extend into the gas as well. These conditions are arbitrary, but they provide a means of matching the experimental conditions. Unfortunately, the experiments we have available for comparison were performed with no knowledge of the details of the gas flow.

Figure 5 shows the pattern of streamlines and the velocity vectors corresponding to the base case operating conditions. Between any two adjacent streamlines in Figure 5(b) the volumetric flow rate is the same, but the mass flow rate changes if the streamlines cross the free surface. Both the pattern of streamlines and the velocity vectors show a clockwise vortex driven in the gas by the counterclockwise recirculation in the liquid phase reservoir. This is a direct consequence of the no-slip boundary condition (6) at the interface. Over this portion of the free surface the evaporation rate is relatively low, mainly owing to a higher concentration of ethanol and water vapour in the overlying gas. Far above the reservoir surface the streamlines indicate a strong vapour current emanating from the thin liquid film. This heightened evaporation is also evident in plots of velocity vectors: the component of velocity normal to the surface, governed by equation (7), increases with distance downstream. Also noteworthy is the viscous boundary layer in the gas phase building downstream of an apparent stagnation point on the free surface (right side, bottom of Figure 5). It is this boundary layer on which we based the model of mass transfer in Section 5. These calculations indicate that the mass transfer model

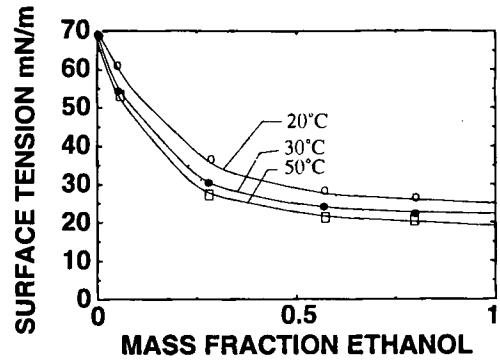

Figure 4. Surface tension versus mass fraction of ethanol in water–ethanol solutions at various temperatures

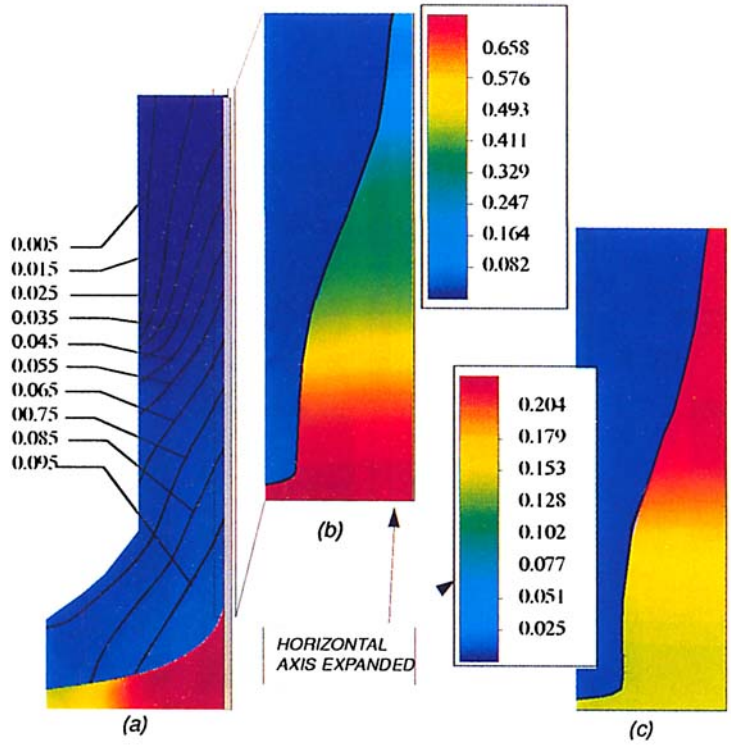

Plate 1. Concentration contours for two-phase flow: (a) mass fraction of ethanol; (b) mass fraction of ethanol in film region; (c) mass fraction of water in film region. The difference between one and the sum of (b) and (c) is the mass fraction of non-volatile species at the same location

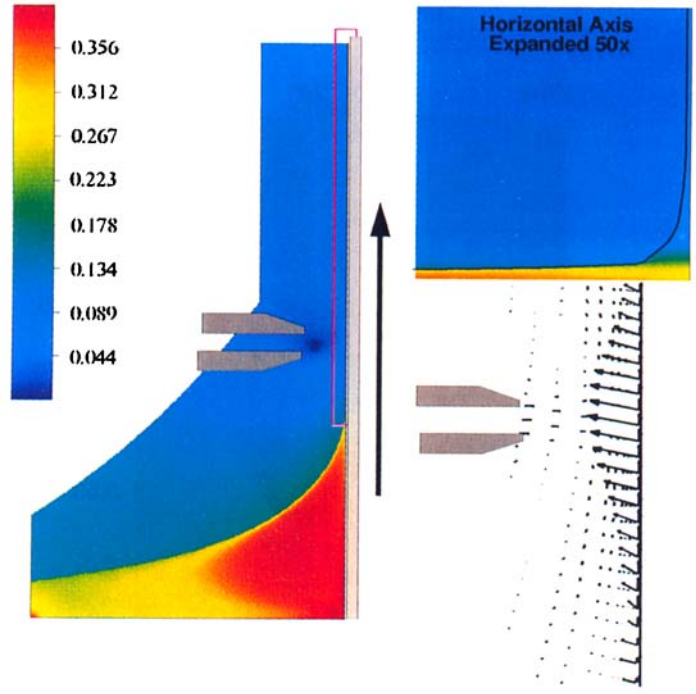

Plate 2. Drying control with air knife. Concentrations are mass fraction of ethanol. Conditions are the same as in previous figures

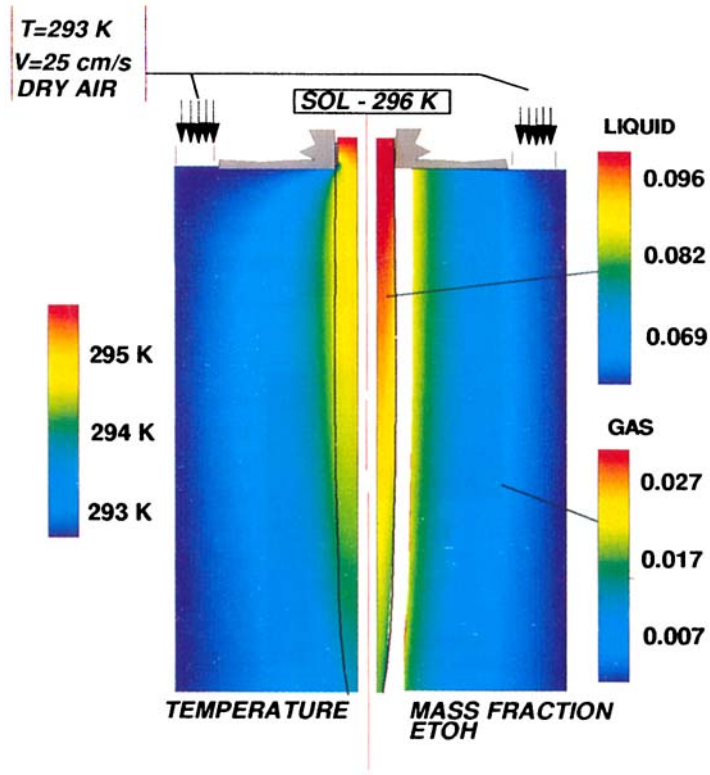

Plate 3. Contours of temperature (left) and mass fraction of EtOH (right) for fibre-spinning base case

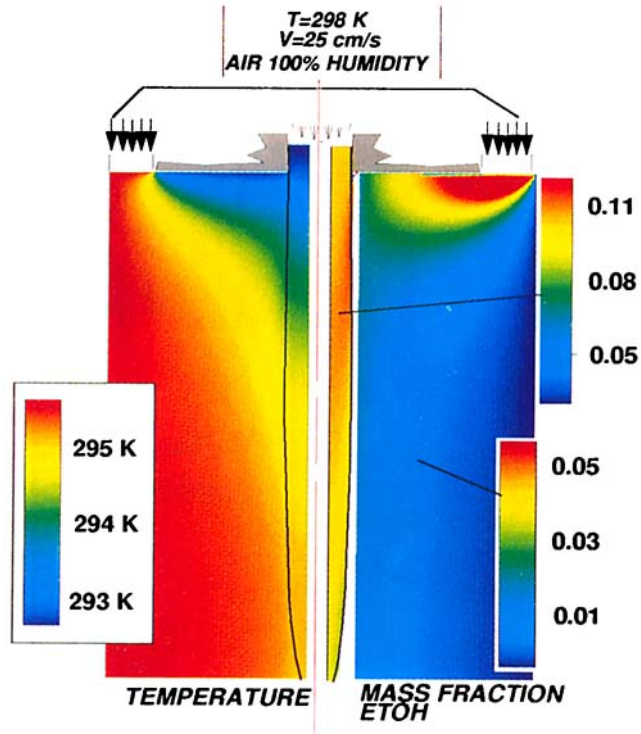

Plate 4. Velocity vectors, isotherms and mass fraction of EtOH for warm, moist inlet air. All other parameters are those of the base case in Table II

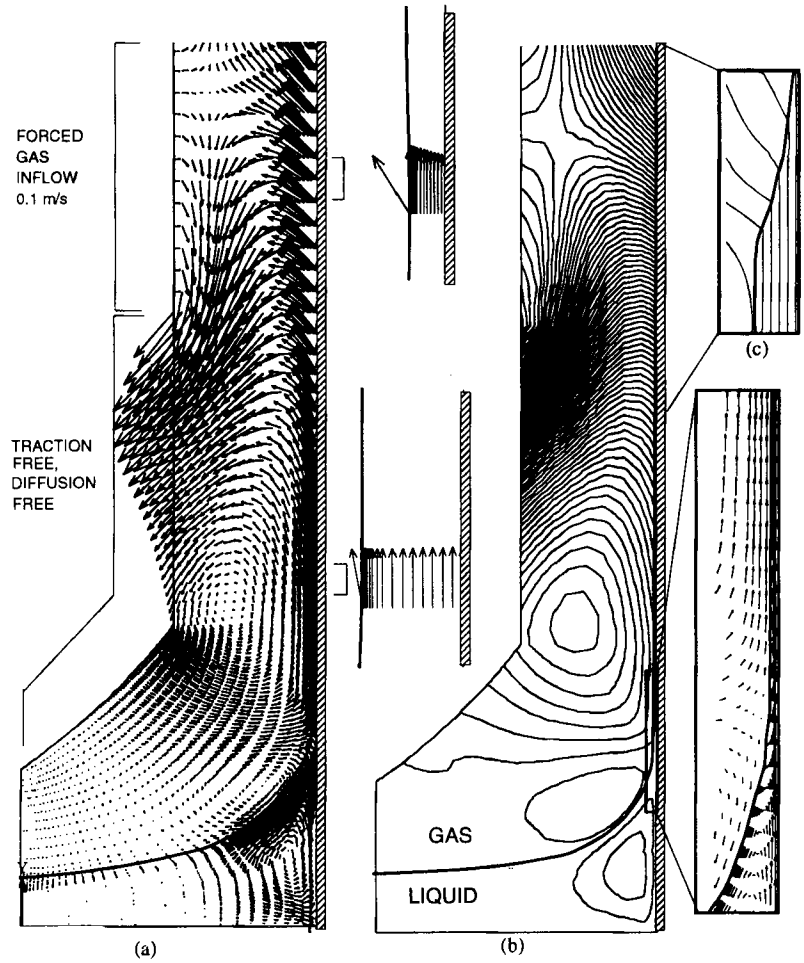

Figure 5. (a) Velocity vectors (absolute) in gas and liquid phases. (b) Pattern of streamlines. (c) Pattern of streamlines in film region with horizontal axis expanded 100 times (multiplied by density)

we employ may be inaccurate in part because of strong convection normal to the free surface.

Vapour–liquid equilibrium conditions make for a concentration discontinuity at the free surface. This discontinuity defines the free surface, as shown in Plate 1. Unfortunately, owing to relatively high vapour pressures, the concentration levels of ethanol and water in the gas phase, and hence the gradients in concentration there, are too small to be resolved by the colour spectrum. For that reason we show an overlay of the concentration contours in the gas phase. Noteworthy is the gradient in concentration normal to the free surface, which grows larger with distance downstream (i.e. contour lines in the gas phase become more parallel to the film downstream), and an apparent layer of relatively high vapour concentration overlying the reservoir (mass fraction 0·095). Correspondingly, we see little enrichment of water and non-volatile species near the reservoir. Well above the reservoir, however, the film becomes depleted in ethanol and the water concentration rises; but the water too is evaporating, and near the outflow plane (projected to be about 2 mm from the drying line) it is overtaken by the

non-volatile species, which begins to concentrate precipitously. Plate 1 shows the mass fraction of non-volatile species rising from 0·4 to 0·7 in the last 1 cm of the film.

When coating binary-solvent-based sols, the meniscus shape usually exhibits a perculiar plateau region followed by a region of rapid thinning and a second, lower plateau. This shape has been observed in earlier experiments,[19] where it was conjectured to be a consequence of differential volatilities and surface tensions of ethanol and water. This mechanism is corroborated by the theory and is shown in Plate 1. Below the second plateau (or 'foot') is a water-rich phase that outlasts the alcohol owing to a lower volatility. This apparent 'phase separation' appears regardless of the original composition of the liquid and over a wide range of drying conditions we tried. It even appears at the evaporation azeotrope composition at which the mixture evaporates at constant concentration.

Surface tension gradients between the alcohol-rich and water-rich portions of the film enhance this plateau region. The velocity vectors in Figure 5 (centre inset) show a rapid acceleration of the surface, and hence of the underlying liquid, towards the downstream plateau, thereby lengthening the foot feature.

Clearly the gas phase plays an important role in the film microstructure development. This makes it possible to control the microstructure via the drying environment. There are several means of doing so, the simplest being with humidity. With the more simplified mass transfer theory for the gas phase, humidity adjustments can be made to the overlying saturation of species i, as we demonstrate in Section 5. Unfortunately, changing the overlying saturation probably alters the flow field and should be accompanied by the appropriate adjustments to the mass transfer coefficient. With the two-phase flow approach, humidity control is a simple matter of placing conditions on the volatile species at the external boundaries of the domain.

As an example we show in Plate 2 the effects of drying control with a narrow jet of dry air impinging on the liquid film just above the level of the reservoir. This approach, often termed *air knife control*, is usually employed to accelerate the drying of films after they are deposited and solidified. Air knives are also commonly employed to control the film thickness through an air-stripping process. Here it is employed to achieve both effects.

The air is blown from a nozzle at 1 m s^{-1} and the coating conditions correspond to the base case outlined in Table I; however, the composition in this case is 40:40:20 water/ethanol/non-volatile species. Plate 2 (right side) shows the velocity field under and around the air knife. Noteworthy is the stagnation-like flow pattern under the jet where it impinges on the film. In this figure the velocity vectors in either phase are multiplied by density, so they indicate a mass flow rate, and the vectors on the free surface in the gas phase have been magnified over the others to show the heightened evaporation underneath the air knife. Plate 2 (left side and top) shows the concentration contours of ethanol in both the gas and the liquid. Here the stagnant layer of gas with high ethanol vapour content is visible beneath the air knife. Up on the substrate the concentration of ethanol in the gas is much less and correspondingly the evaporation rates are much higher. The highest evaporation rates are directly under the air jet at the film surface, as expected, Correspondingly the volatile components are drawn off the film more rapidly, with the film becoming virtually depleted of the more volatile ethanol underneath the air jet. Of course this affects the final film thickness, but not as much as the metering effect through impingement pressure. This is also evident in Plate 2 (top right), where there appears a depression in the film underneath the jet.

Clearly the film concentration and thickness evolution can be controlled with the air knife. If the results we present here are not desirable to a coating practitioner, we are free to vary the concentration of the air blown through the jet. In fact it is possible to enrich the film in a condensable solvent component, as has been demonstrated in the Marangoni drying technique.[20,21]

Sol–gel fibre spinning

Sol-gel fibres can be formed by drawing them directly from viscous sols at room temperature,[17] as shown in Figure 1(b). The two main applications for these fibres are composite reinforcement and refractory textiles. Even though these applications are most efficient when as many as 10–100 fibres are drawn simultaneously, there is much to be learned from the spinning (drawing) and subsequent drying of a single fibre strand. As in sol–gel film formation, drying conditions (gas phase air conditioning) have enormous implications on the final fibre microstructure.

The system we consider here consists of a single fibre strand extruded from a nozzle, with air being forced into the system around the periphery of the nozzle (Figure 1(b)). Insofar as the fibre is extruded vertically, the situation is symmetric about the fibre centreline and so axisymmetric analysis is warranted. The thermophysical properties we consider correspond to a silica-based sol and are listed in Table II. The liquid is taken to be Newtonian, although the viscosity can be a function of temperature. The viscosity here is assumed to vary exponentially with the inverse of temperature,

$$\eta = \eta_0 e^{E_T(1/T - 1/T_0)}, \tag{25}$$

where η_0 is the reference viscosity at the reference temperature T_0 and E_T is a parameter that can be fitted to experimental data. The vapour phase diffusion coefficients are assumed to be constant, but the solute–solvent diffusivity is usually taken as a function of concentration in the liquid phase. The latter is necessary to model a phenomenon known as case hardening, where a layer of dry, non-volatile material forms on the surface of a wet fibre or film, thereby impeding further drying of the material. An empirical concentration dependence is used,

$$D = D_0 e^{A(X_s - X_{s0})}, \tag{26}$$

Table II: Operating conditions and thermophysical properties for fibre-spinning base case

Operating conditions	
Liquid composition (volume %)	10:60:30 EtOH: water: non-volatile species
Inlet liquid temperature	295 K
Mean extrusion speed	1 cm s^{-1}
Nozzle radius	60 μm
External air speed	25 cm s^{-1}
Inlet air composition	Dry
Inlet air temperature	293 K
Thermophysical properties	
Liquid viscosity	8 Pa s
Gas viscosity	$1{\cdot}8 \times 10^{-5}$ Pa s
Liquid density	1000 kg m^{-3}
Gas density	1 kg m^{-3}
Surface tension (equilibrium 20 °C)	50 mN m^{-1}
Liquid diffusivity	1×10^{-8} m^2 s^{-1}
Gas diffusivity	$1{\cdot}6 \times 10^{-4}$ m^2 s^{-1}
Liquid thermal conductivity	0·14 cal s^{-1} m^{-1} K^{-1}
Gas thermal conductivity	$5{\cdot}8 \times 10^{-3}$ cal s^{-1} m^{-1} K^{-1}
Liquid heat capacity	1000 cal kg^{-1} K^{-1}
Gas heat capacity	250 cal kg^{-1} K^{-1}
Heat of vaporization	$5{\cdot}9 \times 10^5$ cal kg^{-1}

where X_s is the mass fraction of solids in the solution, X_{s0} is the reference mass fraction, D_0 is the diffusion coefficient at the reference mass fraction and A is a parameter that can be fitted to experimental data.

Plate 3 shows the pattern isotherms (left) and concentration (right) in both gas and liquid phases for the base case. The ethanol mass fraction drops within the fibre with distance down the spin line. Correspondingly the fibre cools owing to latent heat effects (by approximately 2 K from nozzle exit to bottom of computational domain, a distance of 2·4 mm). Plainly visible are the concentration and temperature boundary layers forming on the gas and liquid sides of the interface. On the gas side the boundary layers of temperature and ethanol vapour grow initially and then are tempered in their growth because of the externally forced flow of dry air. On the liquid side of the interface the concentration boundary layer initially spans the entire fibre cross-section. Although not shown, the concentration boundary layer for the less volatile component (water) steepens along the interface with distance down the spin line, mainly owing to the plummeting diffusivities as the concentration of non-volatile phase (solid fraction) increases (equation (26)). These nearly solid-like diffusion coefficients put stringent requirements on the grid resolution as the concentration boundary layers become exceedingly thin. Here the two-level grid resolution approach we use is a breakthrough. Figure 2 shows that our discretization for convective diffusion is highly refined along the free surface.

To demonstrate the versatility of the two-phase approach, we changed the drying conditions around the fibre. The air temperature at the inflow was increased to 298 K and the air was taken as saturated in ethanol at atmospheric (ambient) temperature and pressure; Plate 4 shows

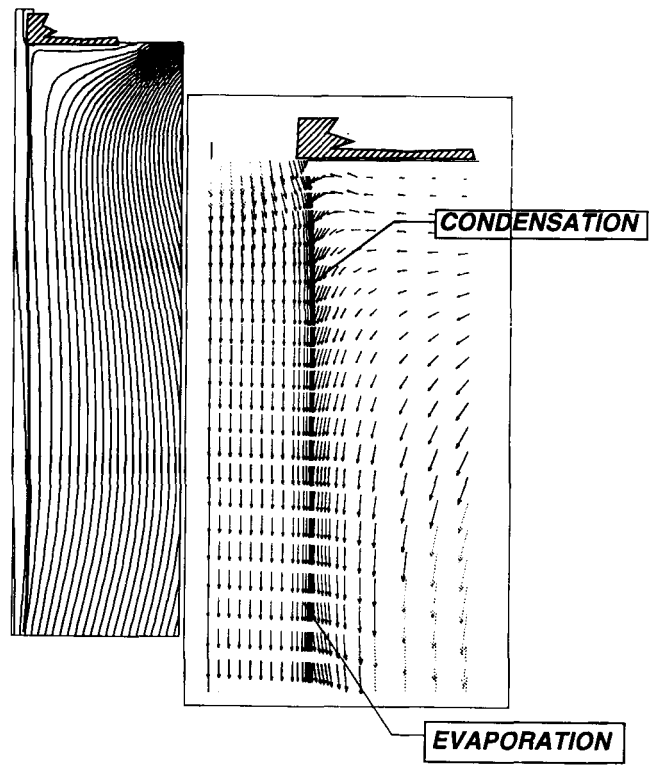

Figure 6. Pattern of streamlines (left) and velocity vectors near nozzle exit (right) for same conditions as in Figure 9

the corresponding isotherms and concentration contours in this case. The thermodynamics conditions here are such that the ethanol initially condenses on the fibre, as indicated by the initial rise in ethanol content in the fibre. Instead of evaporative cooling, the fibre temperature increases initially. Once the ethanol content in the fibre exceeds that needed to reverse the equilibrium, the ethanol begins to evaporate (about half-way between the inflow and outflow). The velocity field, shown in Figure 6), also indicates that condensation is followed by evaporation, since the direction of the velocity relative to the interface reverses about half-way down the spin line. The pattern of streamlines shows that a vapour current does not emanate from the fibre initially, but begins to build far downstream.

These results point out that gas phase conditioning is crucial to controlling the fibre-drying process. It is common practice in many industrial applications to manage the composition and temperature of the gas phase throughout a fibre-spinning tower via multiple intakes and exhaust ports. A similar analysis of localized fibre drying is a straightforward extension of the results presented here and would be akin to the air knife example we covered earlier (see Plate 2). In the next section we demonstrate how difficult it is to tune the less expensive mass and heat transfer coefficient approach, not only to perform the same type of drying control analysis but also to attain agreement between theory and experiment.

5. COMPARISON WITH EXPERIMENT AND SINGLE-PHASE FLOW THEORY

Comparison with experimental data

The two-dimensional model of sol–gel dip coating described above was tested against the film thickness and concentration profiles measured by Brinker *et al.*[22] Recall that the coating liquid in the theory was composed of 74% by weigh ethanol, 16% by weight water and 10% by weight non-volatile species, the last having a molecular weight of 46 g mol^{-1}. In the experiments the liquid was 82% ethanol and 18% water, so the ratio of ethanol to water was the same. The non-volatile component was included in the theory to prevent complete evaporation of the film, a phenomenon the current numerical scheme is incapable of handling. Experiments were performed at coating speeds of 0·2 cm s^{-1}; the computations ranged from 2 to 1 cm s^{-1}. Solutions to the theory at lower coating speeds could not be attained owing to insufficient streamwise resolution in the computational mesh needed to resolve film thicknesses of less than 1 μm.

Figure 7 shows a comparison between film thickness profiles predicted by the theory and the profile measured by imaging ellipsometry. Clearly there is a large discrepancy in the magnitude of the film thickness at any point along the substrate. However, the solution family parameterized by the substrate speed shows that the correct magnitude is apparently being approached with a reduction in substrate speed, which is encouraging. Even more encouraging is that the shape features we predict are similar to the experimental data. It is also reasonable to expect quantitative agreement had we been able to match the conditions of the experiment. We do not expect, however, to be able to predict the exact location of the drying line by the theory unless we can match the drying environment in the experiments and account for the microscale physics which dominates when the film becomes thinner than 100 Å. Unfortunately, at the time of the experiments, little effort was made to characterize the gas flow. This clearly leaves room for future work.

We also checked the predicted concentration profiles against those inferred from fluorescence spectroscopy measurements.[2] Even though the experiments were performed under different conditions, we observed similar concentration variations along the film, with much of the ethanol

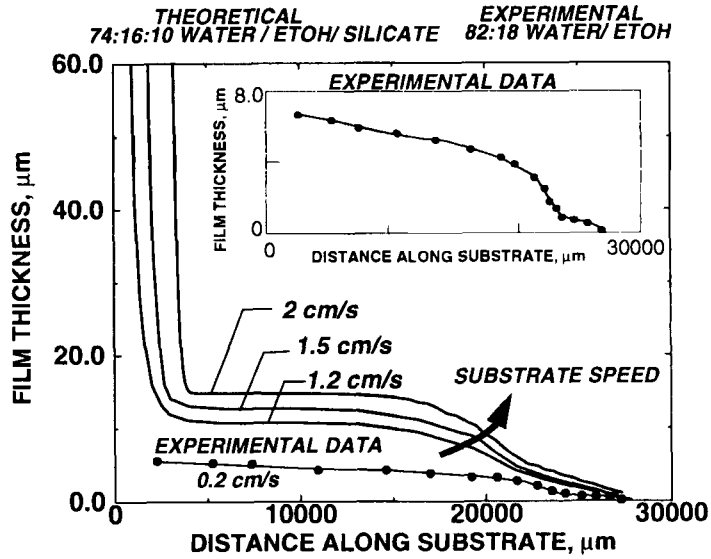

Figure 7. Comparison of theory and experiment

depletion taking place well above the reservoir surface. Unfortunately, at the time of this writing, we had no quantitative measurements available indicating the magnitude of these variations.

Single-phase flow with mass transfer model

The equations of overall mass, momentum and species transfer were also solved in the liquid phase only, with a mass transfer model accounting for the fluid mechanics and mass transport in the gas phase. In this approach the right-hand sides of equations (12) and (13) were replaced by expressions based on the effective flux of each species across the interface. These expressions were of the form $n_i = K_i(X_i - X_i^0)$ for each species i. The constants K_i we estimated from the classical boundary layer theory of semi-infinite flow driven by a moving flat plate emanating from a slit.[23] Figure 8 shows that the boundary layer in the gas phase that builds up downstream of the stagnation point in dip coating is of this type. In this boundary layer approach, functional forms for the velocity components and the concentration are substituted into the Navier–Stokes system and the convective diffusion equations in the gas phase. The resulting equation set is then solved for the rate of mass transfer in terms of the concentrations (partial pressure) of the transported species at the surface of the film. The average gas phase coefficient of mass transfer, K_i, resulting from this approach is

$$K_i = \frac{D_i}{L}(0{\cdot}56Sc_g^{1/2}Re_g^{1/2}), \tag{27}$$

where Re_g is the effective Reynolds number in the gas phase based on the substrate speed and a development length L along the film and Sc_g is the Schmidt number in the gas phase based on the binary diffusivity D_i, taken in this case to be the same for all species. It is noteworthy here that K_i is independent of the local interfacial concentration and that only through the mass transfer model for the flux, i.e. $n_i = K_i(X_i - X_i^0)$, can it depend on the local concentration X_i^0

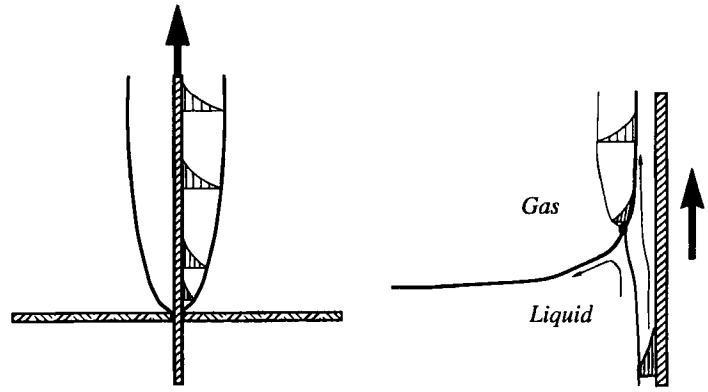

Figure 8. Boundary similarity between moving flat plate and free surface movement in dip coating

in the 'far field' of the gas phase. Furthermore, the local mass transfer coefficient decreases with increasing distance downstream, which leads to lower mass transfer rates.

Figure 9 shows the pattern of streamlines and the corresponding concentration contours for a composition of 82:8:10 ethanol/water/non-volatile species. The streamlines indicate the inflow along the substrate at the bottom of the reservoir. Near the free surface the streamlines also indicate vigorous evaporation, since several intersect the surface. The corresponding concentration contour (top) show streamwise depletion of the more volatile species (ethanol) and a boundary layer of ethanol-lean (water-rich) solution along the free surface overlying the more-or-less static reservoir. This boundary layer turns parallel to the film direction when the film becomes so thin that the substrate presence influences the evaporation-induced concentration gradients. Streamwise enrichment of the non-volatile species is also evident. The concentration contours in this case are largely perpendicular to the interface where the film is thin.

The results in Figure 9 show small variations in volatile species concentration along the free surface. In fact the ratio of water to ethanol remains large (water-rich) and unchanged near the surface, although the absolute mass fractions of these species change as the non-volatile species concentrates along the substrate. This is a result of the constant mass transfer coefficient used so far, which outweighs any mechanism in the liquid phase that might cause the concentration at the surface to vary. Unfortunately the simplified boundary layer theory we employ disallows any mechanism that might lead to a mass transfer coefficient that varies along the film. With this approach we found no way to reproduce the experimentally measured profiles of ethanol–water films.

To investigate the effect of a varying coefficient, we presumed that the evaporation rate must increase with distance downstream, as necessitated by the geometrical effects near the drying line. Correspondingly we tried ramping, in various degrees, the mass transfer coefficient with distance along the surface from the pool to the outflow plane. The results of one case are shown in Figure 10 (left). In this case the mass transfer coefficient was ramped from a low value (one-tenth of that given by Equation (27)) to the value used in Figure 9 over the last 0·2 mm of the entrained film. Now not only is a substantial gradient of ethanol concentration apparent along the free surface, but the corresponding surface tension gradient directed upwards is strong enough to create a small pile-up of water-rich liquid near the outflow plane. On the right of Figure 10 we show the effect of adding a 30% overlying saturation of ethanol in the overlying gas, i.e. we set the partial pressure of ethanol to be 30% of its equilibrium vapour pressure. In this case we notice that evaporation of ethanol is impeded enough to undermine the streamwise depletion of ethanol. In fact the mass fraction of ethanol is still 0·4 at the outflow plane.

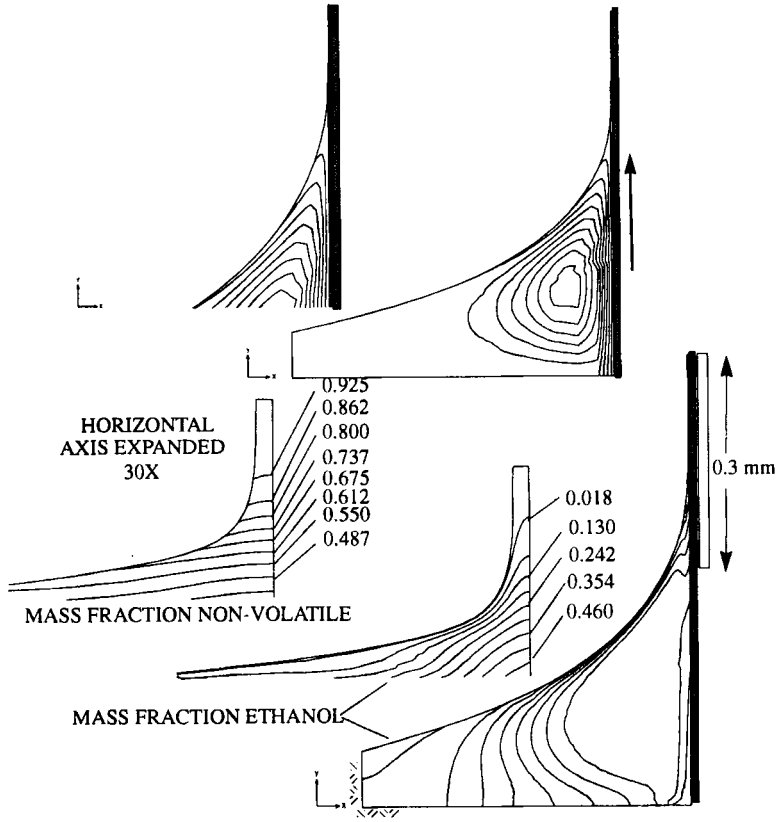

Figure 9. Pattern of streamlines (top) and concentration contours (bottom) predicted with mass transfer model. The mass transfer coefficient (given by equation (27)) is constant along the free surface. Composition is 82:8:10 ethanol/water/non-volatile species

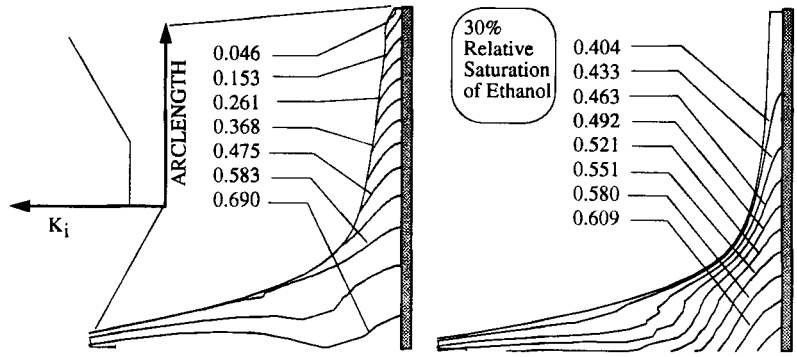

Figure 10. Effect of ramping of mass transfer coefficient (left) and humidity change (right). All other conditions are the same as in Figure 13. The horizontal axis is expanded 30-fold

What this mass transfer analysis shows is that the concentration fields in the entrained film are extremely sensitive to the drying environment. Rather than search for gas phase mass transport theories that account for realistic variations in mass transfer coefficient, and especially theories that are analytically tractable, we opted for a more accurate two-phase approach (Section 4).

6. CONCLUSIONS

In this paper the complicating effects of evaporation and condensation in two industrially important processes were investigated with a realistic model based on conservation laws of overall mass, momentum, species and energy transport. The theory encompasses both gas and liquid phases, with proper interphase boundary conditions applied where appropriate. Multiple components and multiple phases together with the volume change accompanying evaporation or condensation make any numerical scheme for solving the governing equations more challenging. The problem is that velocity and concentration are discontinuous (multivalued) at the surface, the first being a result of a volume expansion that accompanies interphase transfer and the second stemming from vapour–liquid equilibrium. The numerical complexities are handled by a flexible finite element method that can deal with unknown free surface shape, interphase mass and momentum transfer and with velocity and concentration shocks.

Dip coating and fibre spinning of sol–gel materials were chosen as model problems. Sol–gels must be represented by multicomponent multiphase models, since they are normally composed of a condensed phase component which may polymerize or aggregate and one or more solvent components which are volatile (e.g. alcohol and water).

The solutions contain detailed information on the meniscus and the distribution of solute in both phases during deposition. We found that differential volatility leads to surface concentration gradients and hence to surface tension gradients that alter the flow and change the meniscus shape. For the first time the peculiar thinning profile found in dip coating, which has been observed experimentally in alcohol–water systems, is predicted theoretically. Moreover, the predictions agree qualitatively with profiles measured by imaging ellipsometry. Because of this agreement, we extended the calculation to different drying environments to demonstrate how drying strategies might be used to control the sol–gel microstructure in both film and fibre formation. This portion of the anlaysis was made feasible only be extending the theory to two-phase flow rather than relying on a mass transfer coefficient to account completely for the gas phase fluid mechanics and convective diffusion regimes.

ACKNOWLEDGEMENTS

The authors thank A. J. Hurd, C. J. Brinker and C. S. Ashley for providing valuable film thickness and concentration profile data. This research was supported in part by the Basic Energy Sciences programme of the DOE and was performed under contract DE-AC04-76-DP00789.

REFERENCES

1. D. E. Bornwide and R. A. Brown, 'The effects of gas phase convection on mass transfer in spin coating,' *J. Appl. Phys.*, **73**, 585–600 (1993).
2. P. R. Schunk, A. J. Hurd and C. J. Brinker, 'Free meniscus coating processes', in S. F. Kistler and P. M. Schweizer (eds), *Liquid Film Coating: Scientific Principles and Their Technological Implications*, Chapman & Hall, New York, 1993, in press.
3. R. B. Bird, W. E. Stewart and E. N. Lightfoot, *Transport Phenomena*, Wiley, New York, 1960, Chap. 21.

4. D. E. Bornside, 'Spin coating,' *Ph.D. Thesis*, University of Minnesota, 1989 (available from University Microfilms International, Ann Arbor, MI).
5. P. R. Schunk, A. J. Hurd and C. J. Brinker, 'Surface tension gradient effects in sol–gel dip coating,' *Spring National Meeting of AIChE*, New Orleans, LA, March–April 1992.
6. R. A. Cairncross, L. F. Francis and L. E. Scriven, 'Competing drying and reaction mechanisms in the formation of sol-to-gel films, fibers, and spheres,' *Dry. Technol. J.*, **10**, (1992).
7. K. Denbigh, *The Principles of Chemical Equilibrium*, 3rd edn, Cambridge University Press, London, 1971.
8. K. N. Christodoulou and L. E. Scriven, 'Discretization of free surface flows and other moving boundary problems,' *J. Comput. Phys.*, **99**, 39–55 (1992).
9. S. F. Kistler and L. E. Scriven, 'Coating flows,' in J. R. A. Pearson and S. M. Richardson (eds), *Computational Analysis of Polymer Processing*, Applied Science, 1983, pp. 244–299.
10. A. F. Emery and J. R. Egolf, 'Finite element analysis of the stresses and consolidation of boehmite gel during the constant rate drying period,' *Proc. 1989 Natl. Heat Transfer Conf., HTD-113*, 1989, pp. 95–104.
11. Yih-O Tu and R. L. Drake, 'Heat and mass transfer during evaporation in coating formation,' *J. Colloid Interface Sci.*, 562–572 (1990).
12. P. R. Schunk and L. E. Scriven, 'Surfactant effects in coating processes', in S. F. Kistler and P. M. Schweizer (eds), *Liquid Film Coating: Scientific Principles and Their Technological Implications*, Chapman & Hall, New York, 1989, in press.
13. D. M. Himmelblau, *Basic Principles and Calculations in Chemical Engineering*, 4th edn, Prentice-Hall, Englewood Cliffs, NJ, 1982.
14. P. R. Schunk, 'Polymer and surfactant additives in coating and related flows,' *Ph.D. Thesis*, University of Minnesota, 1989 (available from University Microfilms International, Ann Arbor, MI).
15. O. C. Zienkiewicz, *The Finite Element Method*, 4th edn, McGraw-Hill, London, 1990.
16. T. J. R. Hughes, *The Finite Element Method*, Prentice Hall, Englewood Cliffs, NJ, 1987.
17. C. J. Brinkler and G. W. Scherer, *Sol–Gel Science*, Academic, San Diego, CA, 1990.
18. L. D. Landau and V. G. Levich, 'Dragging of a liquid by a moving plate,' *Acta Phys. Chim., URSS*, **17**, 42–54 (1942).
19. A. J. Hurd, 'Evaporation and surface tension effects in dip coating,' in H. Bergna (ed.), *Advanced Chemical Series*, No. 234, *Colloid Chemistry of Silica*, American Chemical Society, Washington, DC, 1992.
20. A. F. M. Leenaars, J. A. M. Huethorst and J. J. van Oekel, 'Marangoni drying: a new extremely clean drying process,' *Langmuir*, **6**, 1701–1703 (1990).
21. S. B. G. O'Brien and B. H. A. A. Van Den Brule, 'A mathematical model for the cleansing of silicon substrate by fluid immersion,' *J. Colloid Interface Sci.*, **144**, 210–221 (1991).
22. C. J. Brinkler, A. J. Hurd, G. C. Frye, P. R. Schunk and C. S. Ashley, 'Sol–gel thin film formation' *J. Ceram. Soc. JN.*, **99**, 862–877 (1991).
23. B. C. Sakiadis, 'Boundary-layer behavior on continuous solid surfaces,' *AIChE J.*, **7**, 26–35 (1961).